NORMA RESEARCH REPORT

T1-D3 (KIAM): (Report M24, 1erMars2022) Smart DDES for acoustics:

Approaches to the Numerical Simulation of the Acoustic Field Generated by a Multi-Element Aircraft Wing in High-Lift Configuration.

A.V. Gorobets, A.P. Duben, T.K. Kozubskaya, P.V. Rodionov(*)

March 2022

(*) CAALAB, Keldysh Institute of Applied Mathematics, Moscow

ISSN 2070-0482, Mathematical Models and Computer Simulations, 2023, Vol. 15, No. 1, pp. 92–108. © Pleiades Publishing, Ltd., 2023.
Russian Text © The Author(s), 2022, published in Matematicheskoe Modelirovanie, 2022, Vol. 34, No. 7, pp. 24–48.

Approaches to the Numerical Simulation of the Acoustic Field Generated by a Multi-Element Aircraft Wing in High-Lift Configuration

A. V. Gorobets[a], A. P. Duben[a], T. K. Kozubskaya[a], and P. V. Rodionov[a,*]

[a] *Keldysh Institute of Applied Mathematics, Russian Academy of Sciences, Moscow, Russia*

**e-mail: pavel.rodionov.cs@gmail.com*

Received February 21, 2022; revised February 21, 2022; accepted March 14, 2022

Abstract—We assess the applicability of the IDDES method for modeling acoustics generated by a multielement aircraft wing with deflected high-lift devices. The testing is carried out using the flow around an unswept wing segment based on the 30P30N airfoil. The near-field acoustics and aerodynamics obtained by the computations are compared with the experimental data. Far-field acoustics is modeled by the FWH method, and the resulting spectra and radiation pattern are presented in the paper. We also test the application of sponge layers on the segment borders as an alternative to the periodic boundary conditions; the corresponding effects on the numerical solution are demonstrated.

Keywords: EBR scheme, DES, 30P30N, validation, sponge layer

DOI: 10.1134/S2070048223010088

1. INTRODUCTION

Reducing the noise generated by a civil aircraft during approach and landing is an urgent scientific and technical task. Its importance is dictated not only by the desire of aircraft manufacturers to increase the comfort of people living in the vicinity of airports but also by the constant tightening of certification requirements imposed by the International Civil Aviation Organization (ICAO) [1]. The development of civil aircraft engines along the path of increasing the bypass ratio has led to a significant reduction in the noise level generated by the engine and the jet flowing from it, and made the airframe an important component of the overall noise generated during approach and landing [2]. The most significant sources of airframe noise are landing gears and deflected high-lift devices such as slats and flaps.

Wind tunnel experimentation is one of the most common and reliable methods for studying the noise of an airframe or its individual elements. With the help of microphone arrays in the far field and the beamforming technique, it is possible to build maps of noise sources for various acoustic frequencies [3]. A similar technique is used during flight tests.

Numerical modeling can be considered as an alternative or additional approach to study airframe noise. In comparison with experiments, this approach has its own advantages and disadvantages. The main advantage is a significantly larger amount of information that can be obtained about the target flow, up to the values of all gas-dynamic parameters at an arbitrary point for each time moment. The advantages also include the possibility of simulating free flow conditions, greater accuracy and flexibility in setting the geometry and a higher degree of repeatability of the results, at least within one computational code. The disadvantages of the approach include possible incorrectness or incomplete correctness due to the assumptions underlying the mathematical models and the presence of numerical errors that arise from the approximation of the original equations. The final computational cost is also important.

Despite the lack of universality of numerical simulation, interest in it from leading scientific and industrial organizations is only increasing. This is indirectly indicated by the large number of international workshops held by the American Institute of Aeronautics and Astronautics (AIAA) dedicated to the validation and development of the applied numerical methods [4]. One of these events is the Workshop on Benchmark problems for Airframe Noise Computations (BANC), which has been held since 2010 [5, 6]. The most recent BANC (BANC-V) workshop took place in 2018 [7].

The focus of BANC workshops is on the numerical study of noise generated by airframe components, such as slats, the trailing edge of the wing, and landing gear. In particular, three-component wing segments without a sweep (sweep angle $\chi \equiv 0$) based on F-15 (DLR) and 30P30N (McDonnell Douglas, DC-10) airfoils are used to study the effect of slats. In the BANC meetings, for these wing segments, experimental data on the distribution of pressure on the surface are provided, and the spectra of pulsations at the points of the near and far fields are given, which makes it possible to test numerical modeling methods both in terms of the correctness of the reproduction of aerodynamics and aeroacoustics of the flow.

To simulate acoustic disturbances generated by the turbulent motion of a viscous fluid, there is a fairly wide range of computational approaches. Direct numerical simulation (DNS) is the most common, but at the same time the most resource-intensive approach among them. It allows to reproduce the acoustics of the target flow solely based on the numerical solution of the Navier–Stokes equations without involving any additional models or assumptions. However, the need to resolve the full spectrum of turbulent fluctuations, up to the Kolmogorov scale, and the corresponding requirements for computational grids, as well as for the time step, make this approach inapplicable or at least devoid of practical meaning when modeling the acoustics of full-scale aircraft components. Less resource-intensive approaches include the large eddy simulation (LES) method. It is based on the use of subgrid viscosity models, which interpret the presence of small-scale turbulence, which is not resolved by the computational grid, as an increase in the fluid viscosity. At the same time, the use of these models gives a physically meaningful result only when the inertial interval of the turbulent spectrum is resolved; i.e., a sufficiently detailed grid resolution is still required, and especially high requirements for the grid arise in areas of the boundary layer, where the corresponding resolution approaches the resolution required for DNS. Thus, at present, LES modeling is also not suitable for reproducing the acoustics of large-scale airframe elements.

The least resource-intensive methods for modeling turbulent flows are those based on solving the Reynolds–averaged Navier–Stokes (RANS) equations. In these methods, all scales of turbulence are modeled by introducing additional variables and equations into the system being solved. The use of turbulence models makes it possible to perform numerical simulations on grids with a very high degree of cell anisotropy, which significantly reduces the requirements for grid sizes and significantly speeds up computations. The use of RANS approaches usually leads to obtaining a stationary flow, although in general, RANS equations allow obtaining large-scale nonstationarity in the solution (unsteady RANS, URANS). In aeroacoustics, RANS modeling is often used as an integral part of the applied methods, in which the description of the dynamics and acoustics of the flow is based on different mathematical models [2, 8, 9]. These methods make it possible to relatively quickly obtain estimates of the acoustic characteristics of the objects under study; however, the degree of reliability of such estimates in some cases is limited.

Reducing the computational cost of LES modeling is possible using hybrid RANS-LES approaches based on the use of RANS modeling near streamlined surfaces and LES modeling in other areas [10]. The most common family of methods of this class, which has been comprehensively tested on industrial-oriented problems [11], is detached eddy simulation (DES) [12, 13]. The improved delayed detached eddy simulation (IDDES) method [14, 15], which combines, depending on the local flow characteristics and grid resolution, the regimes of LES, wall-modelled LES (WMLES) and URANS, is one of the modern non-zonal representatives of the DES family. The IDDES method has been successfully tested on aeroacoustic problems [6, 11].

In this study, the IDDES method implemented in the NOISEtte code [16–18], is tested on the flow around a straight (with sweep angle $\chi \equiv 0$) wing segment 30P30N [6, 19–26], and the resulting aerodynamics and aeroacoustics of the flow are compared with the experimental data.

It should be noted that in this problem, due to the symmetry in the spanwise direction of the time-averaged flow, it is possible to use periodic boundary conditions at the sides of the streamlined segment. At the same time, in many practical problems, for example, the flow around a swept wing ($\chi_{\text{PC.}} \neq \chi_{\text{c.c.}}$), there is no such symmetry, which often leads to the consideration of the full formulation of the problem, when the computational domain contains the entire geometry, not just its characteristic part. The size of the entire geometry can be orders of a magnitude larger than the size of the characteristic area or region of interest, which increases the computational cost of the corresponding simulation by a factor. To reduce the computational cost, it is possible to use additional techniques, one of which is sponge layers [27–30]. Their main idea is to combine the results of more economical RANS simulations with the results of eddy-resolving simulations at each time step in specific areas. This makes it possible to carry out expensive eddy-resolving modeling only in areas of practical interest with extracting the required flow parameters at their boundaries from the RANS solution. In this paper, we study the possibility of using the technique of sponge layers in the flow around a straight wing segment.

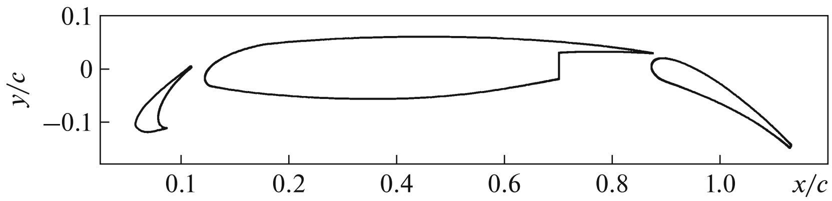

Fig. 1. Geometry of the 30P30N airfoil.

2. EXPERIMENTAL SETUP

A rectangular segment of a three-element wing based on the 30P30N airfoil with flap and slat extended at 30° (Fig. 1) is placed in a free flow at different angles of attack and studied for aerodynamic and acoustic characteristics [23]. The characteristic length for the chosen configuration is the chord of the wing with the slat and flap retracted, hereinafter, denoted by c and equal to 0.457 m. The width of the wing segment in the experiment is $2c$. The slat chord length is about $0.15c$; and that of the flap, about $0.3c$. The free flow Mach number is 0.17, which corresponds to the flow velocity $U_\infty = 58$ m/s. The Reynolds number calculated from the wing chord c is $\mathrm{Re}_c = 1.7 \times 10^6$.

In this paper, we consider the flow characterized by the angle of attack $\alpha = 5.5°$ and a temperature of $T_\infty = 300$ K; these parameters were used in the numerical simulations whose results were reviewed in [6].

During the experiment, the pressure coefficient (C_p), lift coefficient (C_l), and drag coefficient (C_d), as well as the spectra of acoustic disturbances at points on the wing surface and in the far field, were measured.

3. MATHEMATICAL MODEL

The methods used in this study are based on the system of Navier–Stokes equations for a compressible fluid

$$\partial \mathbf{Q}/\partial t + \nabla \cdot \mathrm{F}(\mathbf{Q}) = \nabla \cdot \mathrm{F}_v(\mathbf{Q}, \nabla \mathbf{Q}), \tag{1}$$

where

$$\mathbf{Q} = \begin{pmatrix} \rho \\ \rho\mathbf{u} \\ E \end{pmatrix}, \quad \mathrm{F} = \begin{pmatrix} \rho\mathbf{u} \\ \rho\mathbf{uu} + p\mathbf{I} \\ (E + p)\mathbf{u} \end{pmatrix}, \quad \mathrm{F}_v = \begin{pmatrix} 0 \\ \tau \\ \tau\mathbf{u} - \mathbf{q} \end{pmatrix}.$$

Here, ρ is the density, $\mathbf{u}$ is the velocity vector, p is the pressure, E is the total energy, and $\mathbf{I}$ is the identity tensor. The viscous stress tensor and the heat flux vector are defined as $\tau = \mu[\nabla\mathbf{u} + (\nabla\mathbf{u})^{\mathrm{T}} - (2/3)(\nabla \cdot \mathbf{u})\mathbf{I}]$ and $\mathbf{q} = -k\nabla T$, respectively, where μ is the coefficient of dynamic viscosity, k is the coefficient of thermal conductivity, and T is the temperature. The value of the dynamic viscosity coefficient is determined according to Sutherland's law. To close system (1), the equations of state of a perfect gas are used

$$E = \rho\mathbf{u} \cdot \mathbf{u}/2 + p/(\gamma - 1), \quad p = \rho R_{\mathrm{sp}} T$$

with the ratio of specific heats $\gamma = 1.4$ and gas constant $R_{\mathrm{sp}} = 287.058$ J/(kg K).

To model turbulence according to the Boussinesq hypothesis, we add the coefficient of turbulent dynamic viscosity μ_t. For stationary computations, we will use RANS simulation with Spalart–Allmaras (SA) turbulence models [31]. Eddy-resolving modeling will be carried out according to the IDDES method with a subgrid scale $\Delta = \tilde{\Delta}_\omega$ [32] and subgrid LES model σ [33].

At the initial moment of time, we set the distribution of turbulent viscosity in the entire computational domain according to the equality $\nu_t/\nu = 1$. The use of this initial condition contributes to the rapid formation of turbulent boundary layers near the streamlined surface. On the surface of the streamlined segment, we set the no-slip condition ($\mathbf{u} = 0$) and adiabatic conditions ($\partial T/\partial \mathbf{n} = 0$, where $\mathbf{n}$ is the normal vector to the surface). Also, on the surface of the segment, we set to zero the value of the kinematic turbulent viscosity ν_t. On the far field boundary of the computational domain, we set the free flow conditions.

4. NUMERICAL METHOD

To approximate convective fluxes in the system of equations (1) we will use the vertex-centered hybrid edge-based reconstruction (EBR) scheme [34–36] for unstructured meshes, which is a combination of the central-difference and upwind schemes, which on translation-invariant meshes (i.e., on meshes that are invariant with respect to a shift by any mesh edge) have the fourth and fifth order of approximation, respectively. Approximation of viscous fluxes will be carried out by the method of local element splittings [37]. For time integration, we use an implicit second-order scheme with Newton's linearization of the discretized equations. We will solve the system of linear algebraic equations within one iteration of the Newton method by the stabilized biconjugate gradient method (BiCGStab) with the ILU0 preconditioner.

5. BOUNDARY CONDITIONS AT THE SEGMENT SIDES

5.1. Periodic Boundary Conditions

The possibility of setting periodic boundary conditions at the sides of a straight wing segment naturally follows from the symmetry in the spanwise direction of the resulting time-averaged flow. Moreover, when using stationary RANS simulation, together with periodic conditions, the width of the streamlined segment can be chosen arbitrarily; and due to the indicated symmetry, the results in each of the cross sections will be identical. For the same reason, for stationary RANS modeling in this problem, it is possible to use a two-dimensional formulation.

When using eddy-resolving modeling, the choice of the width of the streamlined segment is limited from below by the maximum width of the interval on which local turbulent pulsations are significantly correlated. If this restriction is violated, periodic conditions will cause the generation of nonphysical turbulent structures, which will lead to a decrease in the accuracy of eddy-resolving modeling. According to both experimental [21] and numerical [38] works, in the problem under consideration, the width at which turbulent fluctuations practically cease to be correlated is approximately $c/9$.

5.2. Sponge Layers

As an alternative approach to setting the boundary conditions at the sides of the segment for the case of eddy-resolving modeling, one can consider the involvement of sponge layers [27–30]. Their application implies a gradual reduction of the results of eddy-resolving simulation in certain zones of the computational domain to a stationary RANS solution at each time step. The reduction rate is chosen from considerations of a multiple decrease in the amplitude of acoustic disturbances propagating within the sponge layer at the time they reach the edge of the computational domain. The main advantage of sponge layers over periodic boundary conditions is the potential generalization to the case of a swept wing segment and other more complex geometries; however, in this paper, we test this technique only for the case of a straight wing segment.

The method of sponge layer implementation described below is a development of the ideas proposed in [30] and is based on direct summation at each time step of the current result of the eddy-resolving simulation and the target stationary RANS solution with some coefficients depending on spatial coordinates. Let us describe the choice of the values of these coefficients.

Without loss of generality, we consider the problem in a one-dimensional formulation. Let $q_n(x)$ be a function that needs to be reduced to the given function $q_{\mathrm{ref}}(x)$ in a certain area. For this purpose, we introduce the differential problem

$$\begin{cases} \partial q/\partial t = -\varphi(x)(q - q_{\mathrm{ref}}), \\ q(x, t_n) = q_n(x), \end{cases} \tag{2}$$

in which the nonnegative function $\varphi(x)$ determines the rate of convergence of the function $q(x,t)$ to $q_{\mathrm{ref}}(x)$ for every point in space. Introducing the replacement $q' = q - q_{\mathrm{ref}}$ and solving system (2), we obtain

$$q' = (q_n - q_{\mathrm{ref}})\exp\left(-\varphi(t - t_n)\right).$$

Thus, the expression for $q_{n+1} = q(x, t_{n+1})$ takes the form

$$q_{n+1} = (1 - \xi)q_n + \xi q_{\mathrm{ref}},$$

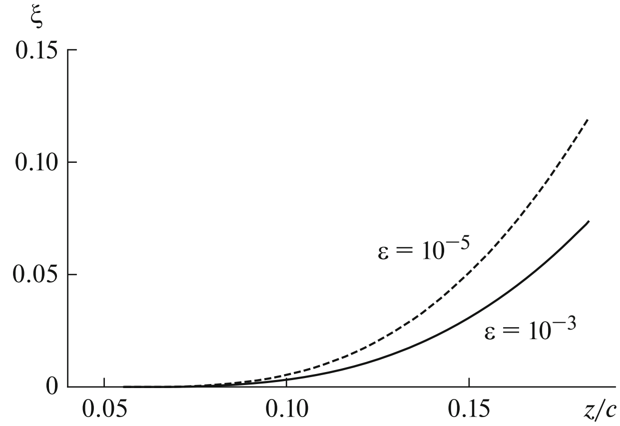

Fig. 2. Examples of distributions of the summation factor ξ inside the sponge layer ($z_1/c = 0.055$, $z_2/c = 0.183$, $\Delta t \times U_\infty/c = 6\times10^{-5}$, $a/U_\infty = 1/\mathrm{M} = 5.88$, $d = 3$).

where $\xi = 1 - \exp(-\varphi\Delta t)$, $\Delta t = t_{n+1} - t_n$. $1-\xi$, and ξ are the desired summation coefficients. Assume

$$\varphi = As^d, \quad s = \frac{x - x_1}{x_2 - x_1}, \quad s \in [0,1], \quad x \in [x_1, x_2],$$

where A, d, x_1, and x_2 are some constants. We define the value of the constant A based on the following reasoning. We consider the damping of an acoustic disturbance with amplitude $\delta(t)$ propagating in the sponge layer from point x_1 to point x_2 at the speed of sound a. It can be expressed as follows:

$$\begin{cases} d\delta/dt = -\varphi(s)\delta, \\ \delta(0) = 1, \end{cases}$$

where $x = x_1 + at$, $s = at/(x_2 - x_1)$. If it is additionally required that

$$\delta\left((x_2 - x_1)/a\right) = \varepsilon,$$

then

$$\delta(t) = \exp\left(-\frac{A(x_2 - x_1)}{(d+1)a}\left(\frac{at}{x_2 - x_1}\right)^{d+1}\right), \quad A = \frac{-\ln\varepsilon(d+1)a}{x_2 - x_1}.$$

Thus, the expressions for the summation coefficients take the form

$$\xi = 1 - \exp(-\varphi\Delta t) = 1 - \exp\left(\ln\varepsilon\frac{(d+1)a\Delta t}{x_2 - x_1}s^d\right), \quad 1 - \xi = \exp\left(\ln\varepsilon\frac{(d+1)a\Delta t}{x_2 - x_1}s^d\right).$$

If the flow in which an acoustic disturbance propagates is characterized by a velocity v in the direction to the sponge layer, a replacement of a to $a + v$ is necessary.

Examples of spatial distributions of coefficient ξ are shown in Fig. 2.

6. METHODS OF CALCULATING THE CHARACTERISTICS OF THE ACOUSTIC FIELD GENERATED BY THE WING SEGMENT

In this study, the acoustic perturbations arising in the flow around the wing segment are estimated in the near and far fields.

The acoustics at the points of the near field is extracted directly from the results of the eddy-resolving simulations after the statistical convergence of the flow by recording the values of the pressure function at equal time intervals. The values of the pressure function at the points are determined by interpolation over the corresponding grid elements. Due to the symmetry of the mean flow along the z axis, the recording is made at several points having the same coordinates (x, y) and separated by equal spatial intervals along the spanwise direction. After the stage of data accumulation for each point using the Welsh periodogram

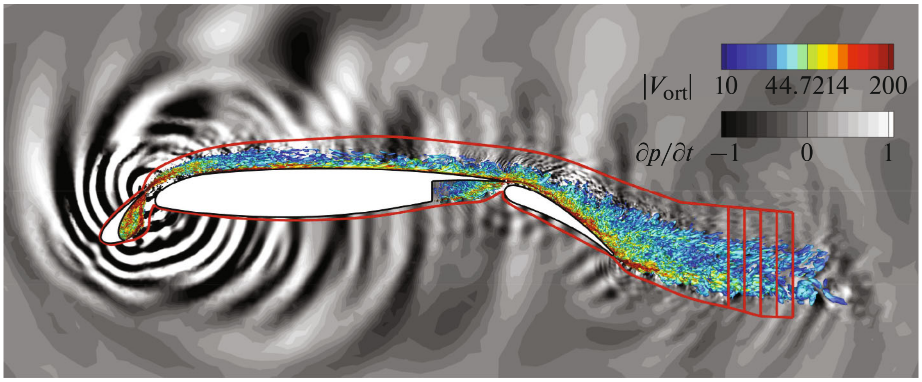

Fig. 3. An example of the location of the FWH surface. The instantaneous flow is illustrated using the field of the time derivative of pressure and Q-criterion isosurfaces corresponding to the value 100, with imprinted vorticity modulus values.

method [39, 40], based on the use of overlapping samples and window functions, which make it possible to obtain smoother spectra at sufficiently short signal recording lengths, and a discrete Fourier transform, the power spectral density of the pressure fluctuations is constructed. The spectra plotted for points with the same coordinates (x, y) are averaged.

The acoustics at the far-field points is calculated based on the results of eddy-resolving modeling by the Ffowcs Williams–Hawkings (FWH) method [41]. Details of the numerical implementation of the method in the NOISEtte code are presented in [42]. When using the FWH method, the additional techniques were used to minimize the loss in its accuracy due to the passage of vortices through the closing surfaces. The first one consisted of averaging the obtained signals using different integration surfaces [43, 44], the second one consisted of using an isentropic substitution [45].

To accumulate the data necessary for the application of the FWH method, near the streamlined airfoil in the plane $(x, y, 0)$, a discrete contour was built with several closures in the wake flow area (Fig. 3). It can be seen that, with the exception of the closing segments, this contour was located in the zone of predominantly linear disturbances. The contour resolution was chosen locally close to the resolution of the basic three-dimensional grid used for eddy-resolving modeling. The constructed contour was extended along the spanwise direction to the width of the eddy-resolving modeling area (when using periodic boundary conditions, to the entire width of the computational domain); the resolution of the resulting discretized FWH surface was also selected to provide closeness to the resolution of the three-dimensional grid. Data were accumulated after the statistical convergence of the flow for the center of each grid element on the FWH surface at constant frequency. Interpolation was used to determine the values of gas-dynamic functions at the centers of surface grid elements. The pressure fluctuations at the far-field points were constructed by applying the FWH method to the data from each combination of an open surface and the corresponding closure. For the obtained pulsations in the far field, the power spectral densities were constructed using the Welsh periodogram method and the discrete Fourier transform; and at coinciding points, these spectra were averaged. The radiation patterns of the propagation of acoustic disturbances were determined based on the obtained pulsations in the far field.

7. COMPUTATIONAL SETUP

In the simulations with periodic boundary conditions, the width of the streamlined segment was chosen to be $0.11c$; and in the simulation with sponge layers, $0.37c$. In both formulations, the computational domain constructed around the wing segment was a straight circular cylinder with a base radius of $150c$. The axis of the cylinder coincided with the z axis and the height was equal to the width of the segment. The position of the segment inside the computational domain was chosen according to Fig. 1.

The three-dimensional grids were built on the basis of two-dimensional grids located in the plane $(x, y, 0)$ by duplicating along the z axis. The parameters of the grids used in this study are given in Table 1 and the characteristic view of these grids in the plane $(x, y, 0)$ is depicted in Fig. 4. Each of the two-dimensional grids was a hybrid one, consisting of quadrangles near the airfoil and triangles in the rest of the domain, with the distance from the airfoil the size of the triangular elements gradually increased. The size of the first near-wall step in all grids satisfies the condition $y^+ < 1$. When constructing meshes Mesh1 and Mesh2, which were used for simulations with periodic boundary conditions, the corresponding two-

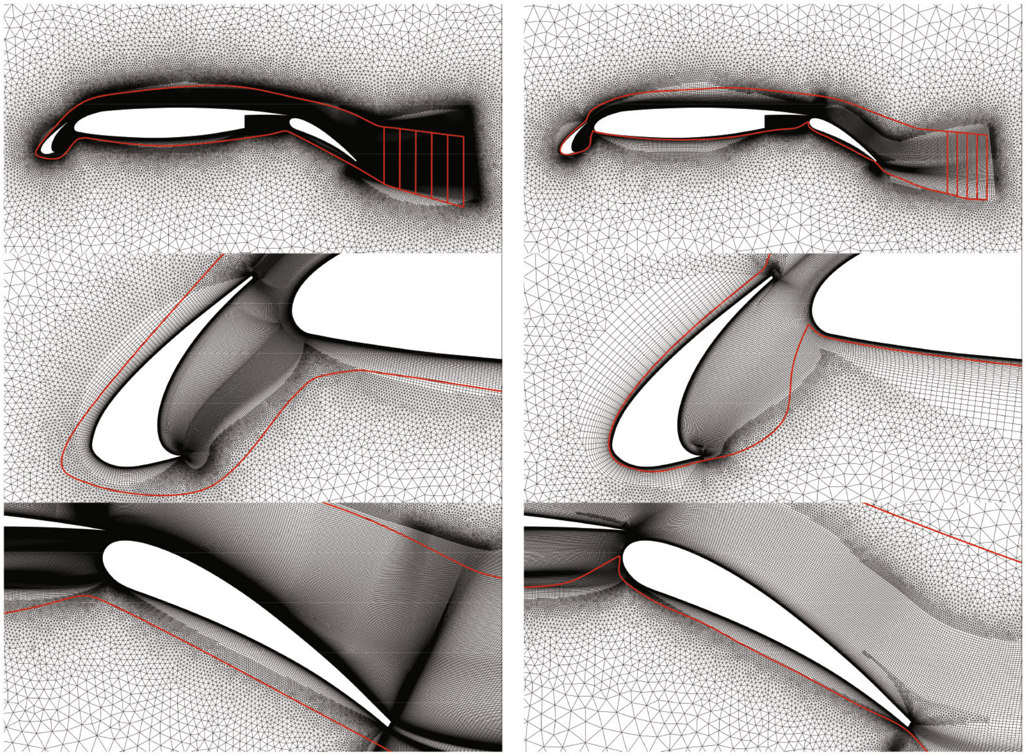

Fig. 4. Computational grids in the $(x, y, 0)$ plane. The contour indicates the location of the corresponding FWH surfaces.

dimensional meshes were duplicated with a constant step along the z axis. The Mesh2Ext mesh used in the simulation with sponge layers coincided with the Mesh2 mesh in the segment $z \in [-0.055c, 0.055c]$; in segments $z \in [-0.183c, -0.055c]$ and $z \in [0.055c, 0.183c]$, the step size along the z axis gradually increased towards the points $z = \pm 0.183c$ by multiplication by a factor of 1.1. In the regions $z \in [-0.183c, -0.055c]$ and $z \in [0.055c, 0.183c]$, the sponge layers were set with parameters $d = 3$ and $\varepsilon = 10^{-3}$.

The acoustics of the near field was evaluated at points P2 and P4–P6 (Table 2, Fig. 5). For subsequent averaging of the spectra, these points were duplicated along the z axis with a step twice as large as the step along the z axis corresponding to the 3D mesh. The position of the FWH surface for each mesh is shown in Fig. 4.

Table 1. Parameters of computational grids

Grid	Number of nodes	Number of nodes in the plane $(x, y, 0)$	Number of nodes along the z axis	Grid width along the z axis
Mesh1	34.9 million	563000	62	$0.11c$
Mesh2	11.4 million	204000	51	$0.11c$
Mesh2Ext	18.6 million	204000	91	$0.37c$

Table 2. Coordinates of points used to evaluate the acoustics of the near field

Designation FSU [24]	Designation JAXA [26]	x/c	y/c
P2	S10	−0.03708	−0.11190
P4	S11	0.005816	−0.007047
P5	S12	0.011533	−0.001677
P6	S13	0.006712	−0.002035

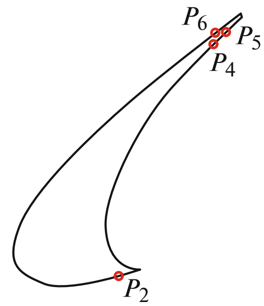

Fig. 5. Location of points used to evaluate the acoustics of the near field.

On the segment $z \in [-0.055c, 0.055c]$, the coefficient for the central difference component of the EBR scheme was assumed to be 0.8 and the coefficient for the upwind component was 0.2. In areas with sponge layers, only the upwind scheme was used. The CFL number in all the computations was 200.

The computational process was organized as follows. First, RANS modeling was carried out on each grid, and the computations were carried out until the lift and drag coefficients were converged. Further, the obtained RANS solutions were used as the initial fields for the corresponding IDDES simulations, as well as for setting the target solutions in the areas of the sponge layers. The stage of data accumulation began after the flow reached the quasi-stationary regime in terms of the lift and drag coefficients: averaged fields, pulsations on the FWH surface, and at points P2 and P4—P6 were recorded during the accumulation process.

The duration of data accumulation on Mesh1 was 50 dimensionless units; and on Mesh2 and Mesh2Ext, 40 and 10 dimensionless units, respectively. Let us give an estimate of the computational cost of the simulation on Mesh2. This computation was carried out on 30 Intel Xeon E5-2690 v4 processors connected via an Infiniband network; one time step took 2.15 seconds in wall-clock time. With the CFL number equal to 200, the time step Δt was about 6×10^{-5} dimensionless units or 5×10^{-7} seconds. Thus, the accumulation of data for 40 dimensionless units required the computation to be performed within 16-and-a-half days.

8. NUMERICAL RESULTS

Figure 6 shows the instant distributions of the z-component of vorticity in the vicinity of the slat obtained from the experiment [24] and simulations on Mesh1 and Mesh2. It can be seen that the general structure of the flow is similar in all cases, but there are differences in the scales of the vortex structures, which is a consequence of the differences in the grid resolution. Figure 7 shows a comparison of the experiment and the computations based on the averaged distributions of the z-component of vorticity. It can be seen that the computational results are close to the experimental data. Similar observations can be made based on Figs. 8 and 9.

Figure 10 compares the experimental [22, 25] and numerical data on the pressure coefficient. It can be seen that almost everywhere the difference between the experiments and computations does not exceed 0.2. The only exception is the area above the slat in the IDDES simulation on Mesh1; the reasons for the significant deviation from the experimental data remain unclear, given the fairly detailed grid resolution in this area. The resulting lift and drag coefficients are summarized in Tables 3 and 4.

The general view of the flow obtained on Mesh2 and Mesh2Ext are shown in Fig. 11. It can be seen that the vortex structures of the developed turbulent flow do not penetrate into the region of sponge layers due to summation with the stationary RANS solution at each time step.

The work of the sponge layers is also illustrated by Fig. 12. Unlike large vortex structures, acoustic disturbances penetrate into the region of the sponge layers; however, according to the equations from Section 5.2, the amplitude of these disturbances gradually decreases when moving towards the boundary of the computational domain. In this illustration, we can also observe the gradual damping of acoustic waves as they propagate in areas with a decreasing grid resolution.

Let us now turn to the consideration of the spectral characteristics of pressure fluctuations at the points of the near and far fields. Note that when processing pressure pulsations, the signal was filtered over the frequency range from 250 Hz to 11.5 kHz. For near-field points, in order to obtain smoother spectra, they

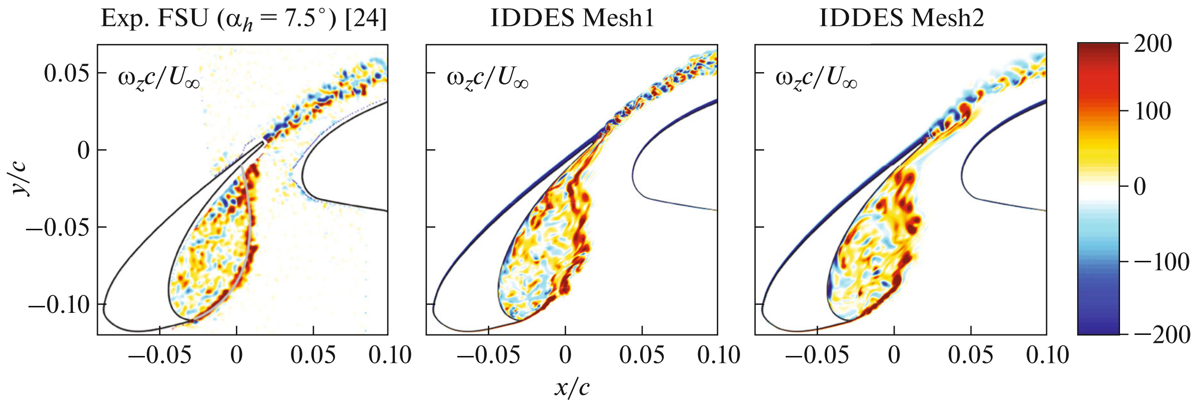

Fig. 6. Instantaneous distributions of the z-component of vorticity.

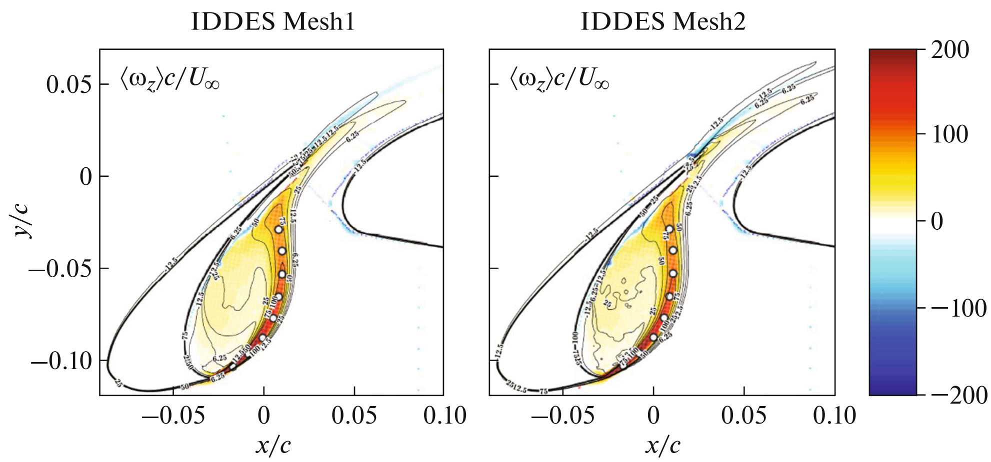

Fig. 7. Average distributions of the z-component of vorticity. On the results of the FSU experiment ($\alpha_h = 7.5°$) [24], the numerical results are plotted by isolines.

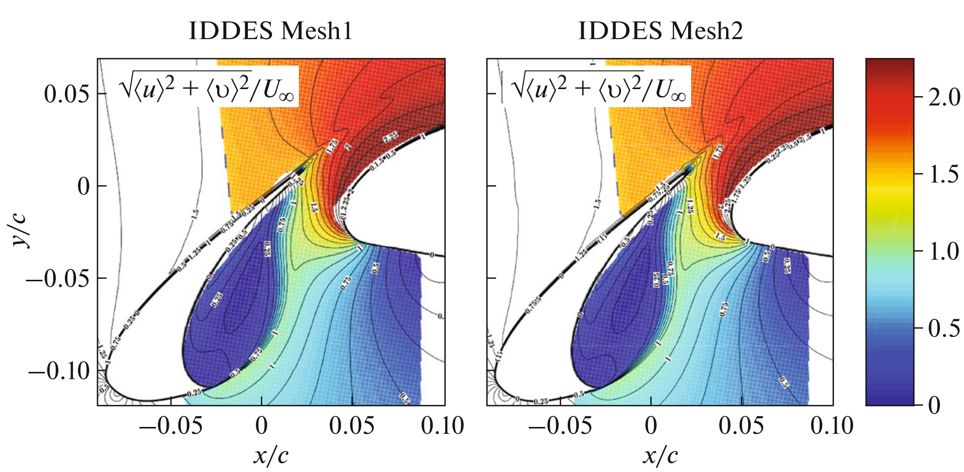

Fig. 8. Averaged distributions of the velocity magnitude. On the results of the FSU experiment ($\alpha_h = 7.5°$) [24], the numerical results are plotted by isolines.

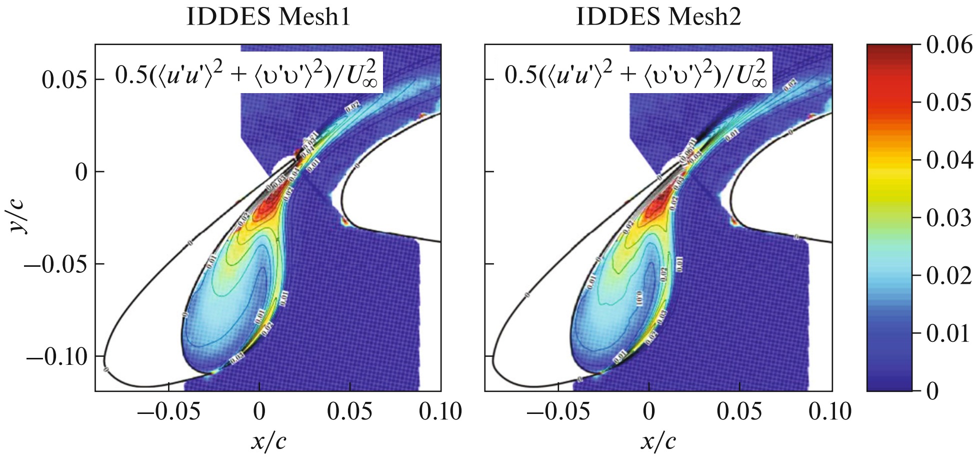

Fig. 9. Averaged distributions of turbulence kinetic energy. On the results of the FSU experiment ($\alpha_h = 7.5°$) [24], the numerical results are plotted by isolines.

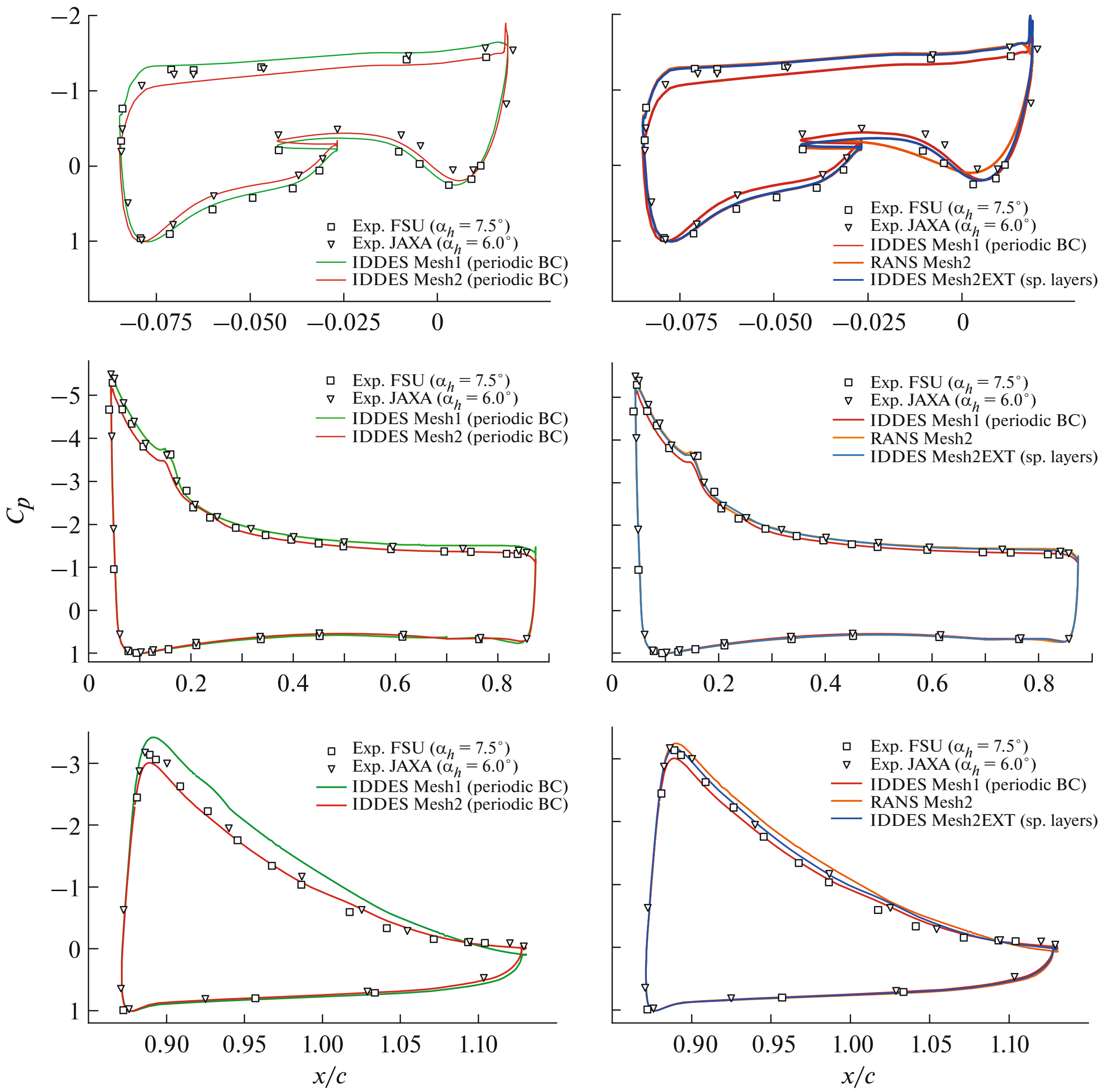

Fig. 10. Pressure coefficient distributions (C_p) obtained from numerical simulations and experiments.

Table 3. Lift coefficients (C_l) based on the length of the chord c in the (x, y) plane

	Slat	Wing	Flap	Total
Exp. FSU ($\alpha_h = 7.5°$)	0.205	2.158	0.477	2.857
Exp. JAXA ($\alpha_h = 6°$)	–	–	–	2.880
IDDES Mesh1 (periodic BC)	0.171	2.315	0.511	2.997
IDDES Mesh2 (periodic BC)	0.149	2.178	0.446	2.775
RANS Mesh2	0.176	2.290	0.484	2.96
IDDES Mesh2Ext (sp. layers)	0.173	2.274	0.471	2.918

Table 4. Drag coefficients (C_d) based on the length of chord c in the (x, y) plane

	Slat	Wing	Flap	Total
IDDES Mesh1 (periodic BC)	−0.088	−0.148	0.286	0.051
IDDES Mesh2 (periodic BC)	−0.063	−0.140	0.251	0.048
RANS Mesh2	−0.094	−0.141	0.272	0.038
IDDES Mesh2Ext (sp. layers)	−0.089	−0.140	0.265	0.036

were averaged along the z axis: in the simulations with periodic boundary conditions, averaging was carried out over the entire width of the domain and in the simulation with sponge layers, only over the high-resolution region $z \in [-0.055, 0.055]$.

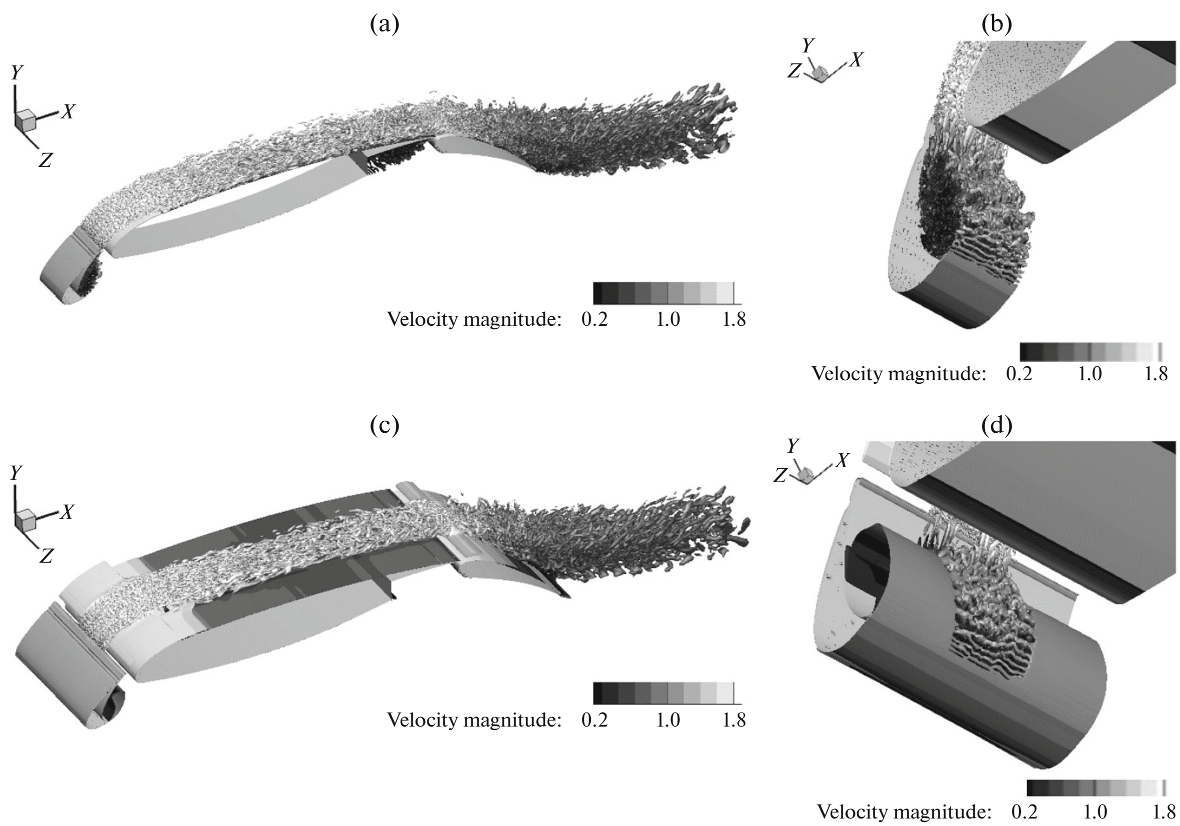

Fig. 11. General view of the flow around a straight wing segment obtained by the simulations with periodic boundary conditions (a, b) (Mesh2) and sponge layers (c, d) (Mesh2Ext). The Q-criterion isosurfaces corresponding to value 100 are shown.

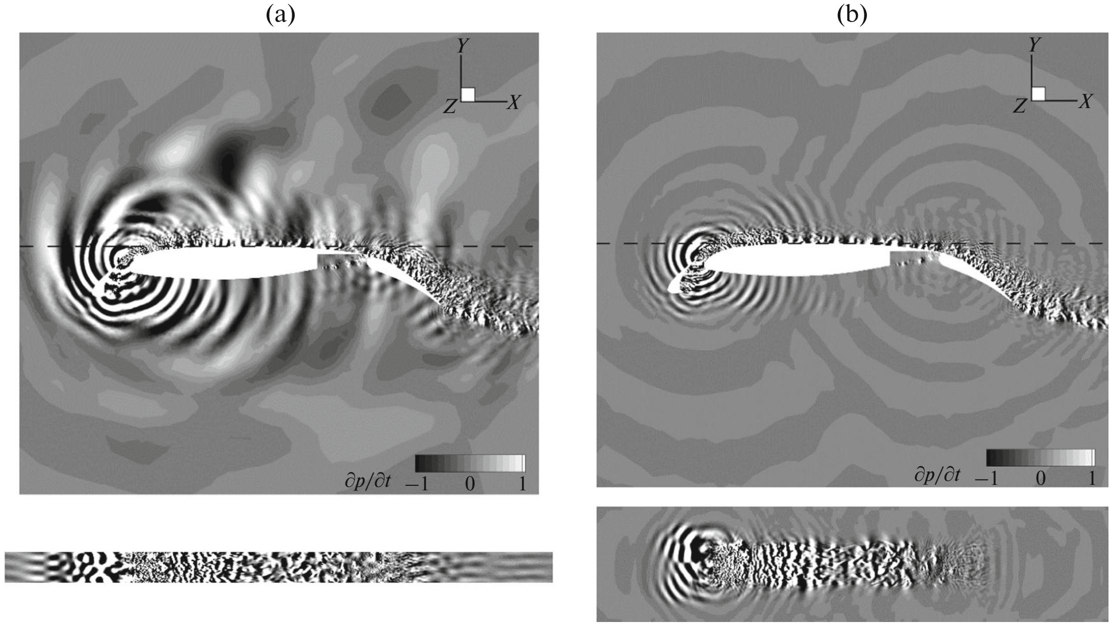

Fig. 12. Instantaneous fields of the time derivative of pressure obtained by the simulations with periodic boundary conditions (a) (Mesh2) and sponge layers (b) (Mesh2Ext).

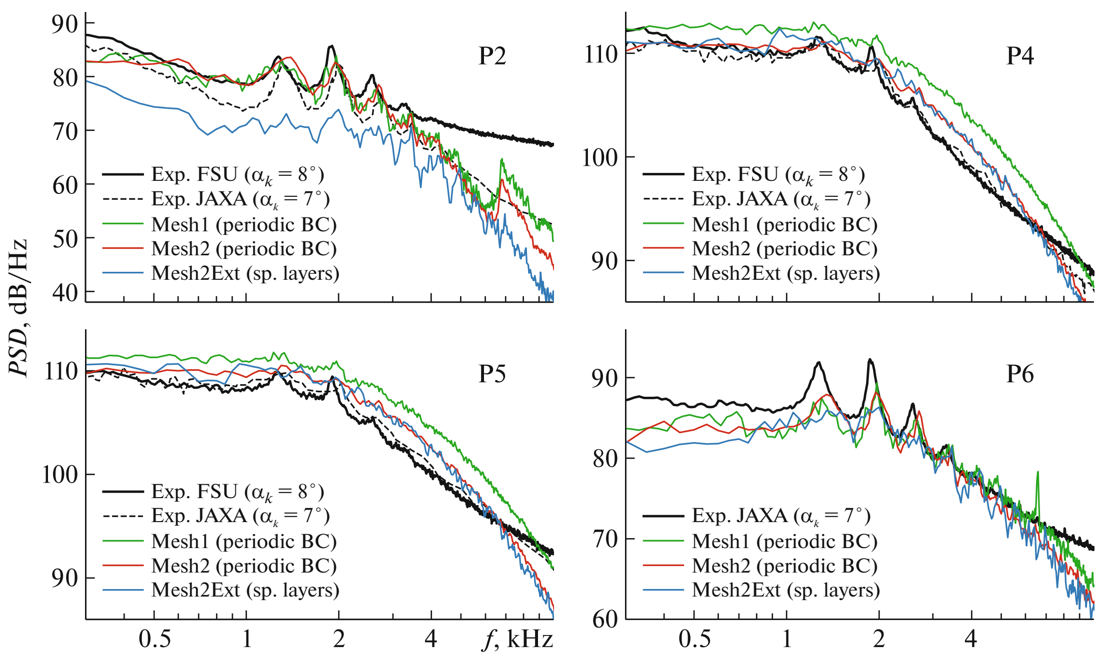

Fig. 13. Power spectral density (PSD) at near field points.

Figure 13 shows the experimental and computational plots of the power spectral density at the points of the near field. It can be seen that at points P2 and P6, the difference between the spectra of the signals obtained on Mesh1 and Mesh2 in the range 1–4 kHz does not exceed 2 dB. Their difference from the experimental spectra in this frequency band does not exceed 4 dB. At points P4 and P5, the deviation of the results obtained on Mesh2 from the experimental data does not exceed 3 dB, while the deviation from the experiment in the results from Mesh1 reaches 6 dB. The difference between the results obtained in the simulation with periodic conditions (Mesh2) and sponge layers (Mesh2Ext), at points P4, P5, and P6 is

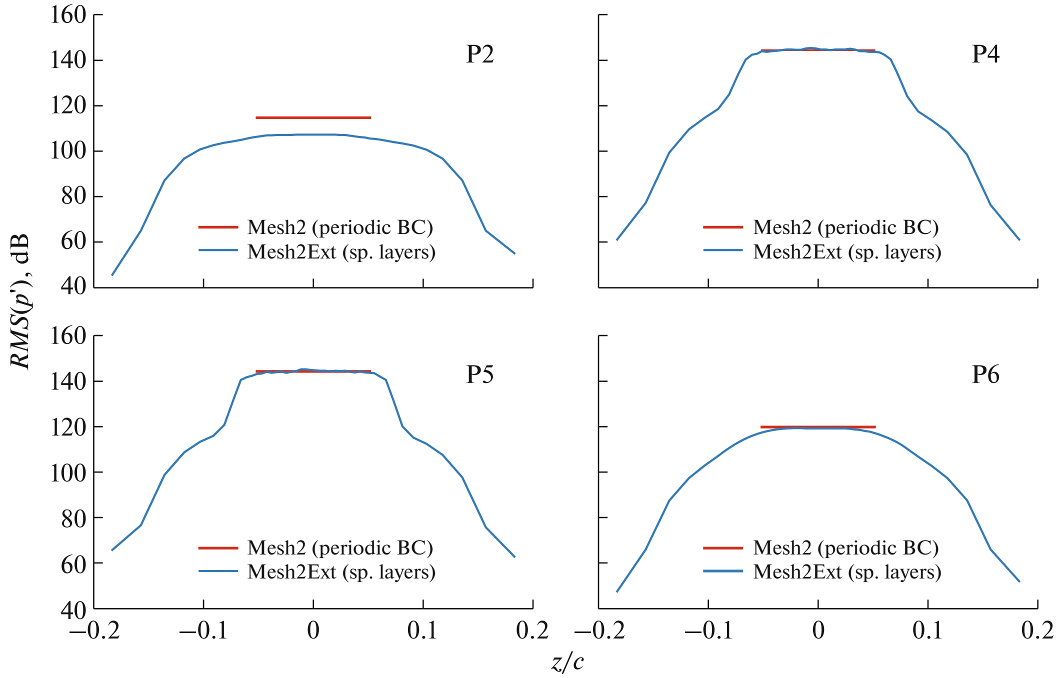

Fig. 14. Distributions of the root mean square (RMS) deviation of pressure in the spanwise direction at the points of the near field.

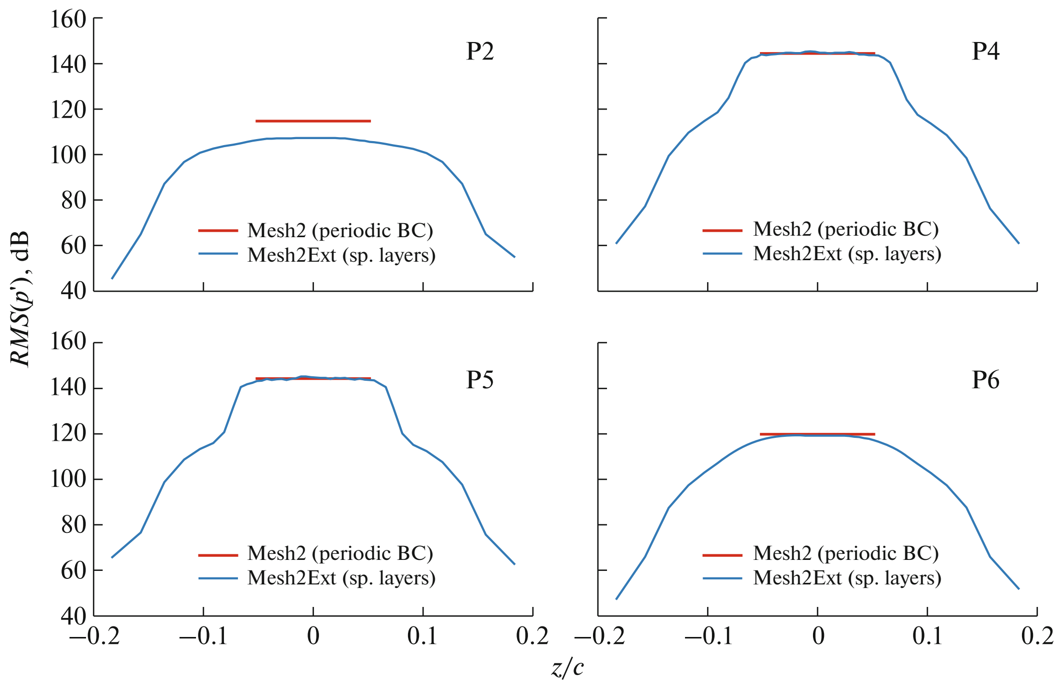

Fig. 15. Distributions of the root mean square (RMS) deviation of pressure in the spanwise direction at the points of the near field.

within 2 dB for almost the entire frequency range. At point P2, these differences reach 10 dB, i.e., as the distance from the source of acoustic pulsations increases, the difference between the two approaches increases noticeably, which may be due to the fact that when using periodic conditions, the flow around an infinite wing is actually simulated, while when using sponge layers, only the flow around the selected segment is modeled. The damping rate of acoustic disturbances propagating inside the sponge layer is illustrated by Fig. 14.

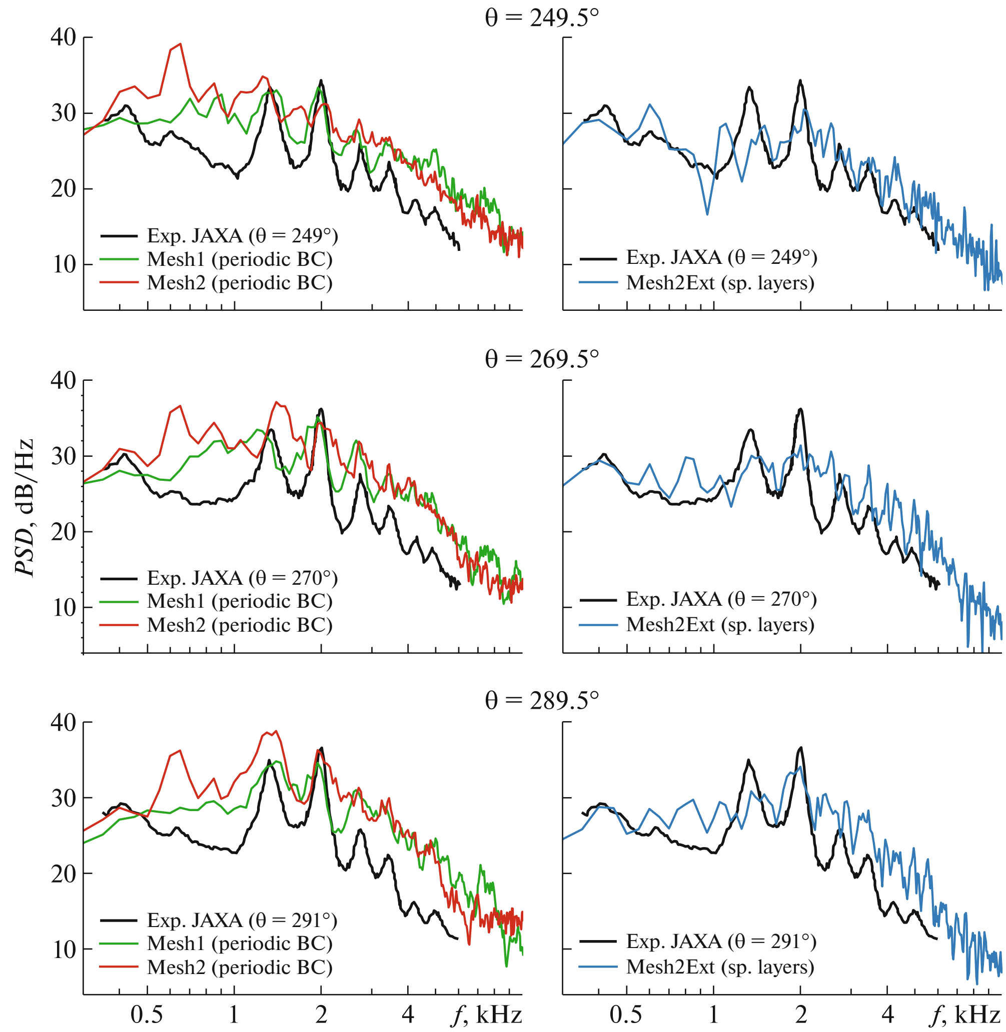

Fig. 16. Power spectral density at far field points.

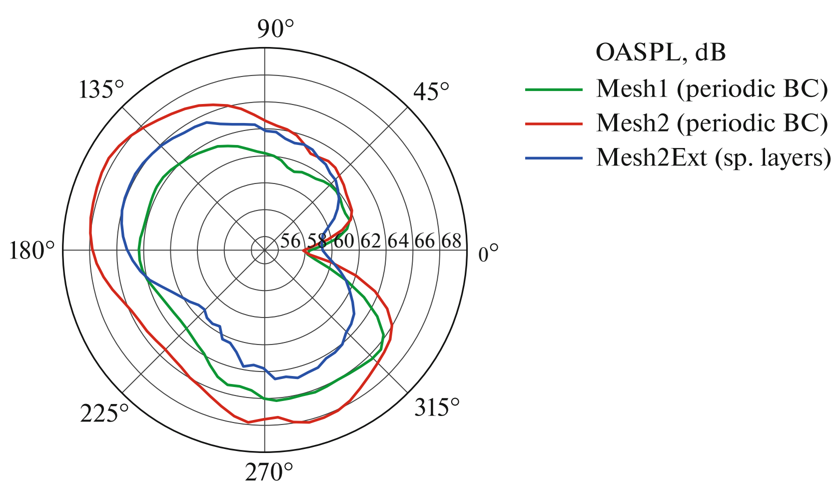

Fig. 17. Radiation pattern for straight wing segment.

To describe the far-field points, we introduce in the plane $(x, y, 0)$ polar coordinates (r, θ) centered at the point (0, 0, 0). We direct axis r parallel to the direction of the free flow. On circle $r = 10c$, let us choose points with coordinates $\theta = 249.5°$, $269.5°$, and $289.5°$ and compute the spectra of acoustic pulsations for them using the FWH method (Fig. 15). For comparison with the experiment, we use the data from [7, 26]. It can be seen that the results of numerical simulations with periodic conditions give a significantly higher level of pulsations compared to the experiment (the difference reaches 8 dB), although the corresponding spectra in the range 1–4 kHz partially repeat the shape of the experimentally observed power spectral density. The spectra obtained in the far field from the simulation with sponge layers turn out to be closer to the experimental values: in the range 1–4 kHz, the differences are about 4 dB, reaching 6 dB for some frequencies. In general, the spectra obtained in the far field on Mesh2Ext contain more spurious noise than the data obtained on Mesh1 and Mesh2, which is probably due to the significantly shorter period of data accumulation. The resulting radiation pattern in terms of angle θ is shown in Fig. 16.

It is difficult to draw any rigorous conclusions about the suitability of sponge layers for modeling far-field acoustics based on the presented results; this issue requires further research.

CONCLUSIONS

This paper shows that the eddy-resolving IDDES method is suitable for numerical simulation of the acoustic field generated by the aircraft wing with deflected high-lift devices during approach and landing. The provided comparisons of the numerical results with the experimental data indicate the correctness of the implementation of the IDDES method in the NOISEtte code. Testing the technique of sponge layers showed the possibility of using them as an alternative to periodic boundary conditions in the case of flow around a non-swept wing segment. Future studies are planned to study the possibility of using the technique of sponge layers in the simulation of the unsteady turbulent flow near the swept wing segment.

FUNDING

The work was supported by the Russian Foundation for Basic Research (project 19-51-80001 BRICS_t). The computations were performed on the hybrid supercomputer K60 installed in the Supercomputer Centre of Collective Usage of KIAM RAS with the additional use of the Shared research facilities of HPC computing resources at Lomonosov Moscow State University.

CONFLICT OF INTEREST

The authors declare that they have no conflicts of interest.

REFERENCES

1. Reduction of Noise at Source. Environmental Protection. ICAO. https://www.icao.int/environmental-protection/pages/reduction-of-noise-at-source.aspx. Cited February 17, 2022.
2. W. Dobrzynski, R. Ewert, M. Pott-Pollenske, M. Herr, and J. Delfs, "Research at DLR towards airframe noise prediction and reduction," Aerosp. Sci. Technol. **12** (1), 80–90 (2008). https://doi.org/10.1016/J.AST.2007.10.014
3. R. Merino-Martínez, P. Sijtsma et al., "A review of acoustic imaging methods using phased microphone arrays," CEAS Aeronaut. J. **10** (1), 197–230 (2019). https://doi.org/10.1007/S13272-019-00383-4
4. AIAA CFD Workshops. https://cfd2030.com/workshops. html. Cited February 17, 2022.
5. M. Choudhari, C. Bahr, M. Khorrami, D. Lockard et al., "Simulations and measurements of airframe noise: A BANC Workshops perspective," in *NATO STO-MP-AVT-246 Specialists' Meeting on Progress and Challenges in Validation Testing for Computational Fluid Dynamics*, p. MP-AVT-246-16 (2016).
6. M. M. Choudhari and D. P. Lockard, "Assessment of slat noise predictions for 30P30N high-lift configuration from BANC-III workshop," in *21st AIAA/CEAS Aeroacoustics Conference, Dallas, TX, 2015*, p. AIAA 2015-2844. https://doi.org/10.2514/6.2015-2844
7. J.A. Housman, G.-D. Stich, J. G. Kocheemoolayil, and C.C. Kiris, "Predictions of slat noise from the 30P30N at high angles of attack using zonal hybrid RANS-LES," in *25th AIAA/CEAS Aeroacoustics Conference, Delft, Netherlands, 2019*, p. AIAA 2019-2438. https://doi.org/10.2514/6.2019-2438

8. M. Herr, R. Ewert et al., "Broadband trailing-edge noise predictions—Overview of BANC-III results," in *21st AIAA/CEAS Aeroacoustics Conference, Dallas, TX, 2015*, p. AIAA 2015-2847. https://doi.org/10.2514/6.2015-2847
9. J. Delfs, L. Bertsch, C. Zellmann, L. Rossian, E.K. Far, T. Ring, S.C. Langer, "Aircraft noise assessment—From single components to large scenarios," Energies **11** (2), 429, 1–25 (2018). https://doi.org/10.3390/EN11020429
10. S. Heinz, "A review of hybrid RANS-LES methods for turbulent flows: Concepts and applications," Prog. Aerosp. Sci. **114**, 100597 (2020). https://doi.org/10.1016/J.PAEROSCI.2019.100597
11. W. Haase, M. Braza, and A. Revell, *DESider—A European Effort on Hybrid RANS-LES Modelling*, Notes on Numerical Fluid Mechanics and Multidisciplinary Design, Vol. 103 (Springer, Berlin, 2009). https://doi.org/10.1007/978-3-540-92773-0
12. P. R. Spalart, "Detached-eddy simulation," Annu. Rev. Fluid Mech. **41**, 181–202 (2009). https://doi.org/10.1146/ANNUREV.FLUID.010908.165130
13. C. Mockett, M. Fuchs, and F. Thiele, "Progress in DES for wall-modelled LES of complex internal flows," Comput. Fluids **65**, 44–55 (2012). https://doi.org/10.1016/J.COMPFLUID.2012.03.014
14. M. L. Shur, P. R. Spalart, M. K. Strelets, and A. K. Travin, "A hybrid RANS-LES approach with delayed-DES and wall-modelled LES capabilities," Int. J. Heat Fluid Flow **29** (6), 1638–1649 (2008). https://doi.org/10.1016/J.IJHEATFLUIDFLOW.2008.07.001
15. M. L. Shur, P. R. Spalart, M. K. Strelets, and A. K. Travin, "An enhanced version of DES with rapid transition from RANS to LES in separated flows," Flow Turbul. Combust. **95** (4), 709–737 (2015). https://doi.org/10.1007/S10494-015-9618-0
16. I. V. Abalakin, P. A. Bakhvalov, A. V. Gorobets, A. P. Duben, and T. K. Kozubskaya, " Parallel research code NOISEtte for large-scale CFD and CAA simulations," Vychisl. Metody Program. **13** (3), 110–125 (2012).
17. A. Gorobets, "Parallel algorithm of the NOISEtte code for CFD and CAA simulations," Lobachevskii J. Math. **39** (4), 524–532 (2018). https://doi.org/10.1134/S1995080218040078
18. A. Gorobets and P. Bakhvalov, "Heterogeneous CPU+GPU parallelization for high-accuracy scale-resolving simulations of compressible turbulent flows on hybrid supercomputers," Comput. Phys. Commun. **271**, 108231 (2022). https://doi.org/10.1016/J.CPC.2021.108231
19. K. Paschal, L. Jenkins, and C. Yao, "Unsteady slat wake characteristics of a 2-D high-lift configuration," in *38th Aerospace Sciences Meeting and Exhibit, Reno, NV, 2000*, p. AIAA 2000-0139. https://doi.org/10.2514/6.2000-139
20. L. N. Jenkins, M. R. Khorrami, and M. Choudhari, "Characterization of unsteady flow structures near leading-edge slat: Part I. PIV measurements," in *10th AIAA/CEAS Aeroacoustics Conference, Manchester, United Kingdom, 2004*, p. AIAA 2004-2801. https://doi.org/10.2514/6.2004-2801
21. K. A. Pascioni, L. N. Cattafesta, and M. M. Choudhari, "An experimental investigation of the 30P30N multi-element high-lift airfoil," in *20th AIAA/CEAS Aeroacoustics Conference, Atlanta, GA, 2014*, p. AIAA 2014-3062. https://doi.org/10.2514/6.2014-3062
22. K. A. Pascioni and L. N. Cattafesta, "Aeroacoustic measurements of leading-edge slat noise," in *22nd AIAA/CEAS Aeroacoustics Conference, Lyon, 2016*, p. AIAA 2016-2960. https://doi.org/10.2514/6.2016-2960
23. K. A. Pascioni and L. N. Cattafesta, "An aeroacoustic study of a leading-edge slat: Beamforming and far field estimation using near field quantities," J. Sound Vib. **429**, 224–244 (2018). https://doi.org/10.1016/J.JSV.2018.05.029
24. K. A. Pascioni and L. N. Cattafesta, "Unsteady characteristics of a slat-cove flow field," Phys. Rev. Fluids **3** (3), 034607 (2018). https://doi.org/10.1103/PHYSREVFLUIDS.3.034607
25. M. Murayama, K. Nakakita, K. Yamamoto, H. Ura, Y. Ito, and M. M. Choudhari, "Experimental study of slat noise from 30P30N three-element high-lift airfoil in JAXA hard-wall low-speed wind tunnel," in *20th AIAA/CEAS Aeroacoustics Conference, Atlanta, GA, 2014*, p. AIAA 2014-2080. https://doi.org/10.2514/6.2014-2080
26. M. Murayama et al., "Experimental study of slat noise from 30P30N three-element high-lift airfoil in JAXA kevlar-wall low-speed wind tunnel," in *2018 AIAA/CEAS Aeroacoustics Conference, Atlanta, GA, 2018*, p. AIAA 2018-3460. https://doi.org/10.2514/6.2018-3460

27. D. J. Bodony, “Analysis of sponge zones for computational fluid mechanics,” J. Comput. Phys. **212** (2), 681–702 (2006).
https://doi.org/10.1016/J.JCP.2005.07.014

28. A. Mani, “Analysis and optimization of numerical sponge layers as a nonreflective boundary treatment,” J. Comput. Phys. **231** (2), 704–716 (2012).
https://doi.org/10.1016/J.JCP.2011.10.017

29. A. Colombo and A. Crivellini, “Assessment of a sponge layer non-reflecting boundary treatment for high-order CAA/CFD computations,” Comput. Fluids **140**, 478–499 (2016).
https://doi.org/10.1016/J.COMPFLUID.2016.09.019

30. G. Ashcroft and X. Zhang, “A computational investigation of the noise radiated by flow-induced cavity oscillations,” in *39th Aerospace Sciences Meeting and Exhibit, Reno, NV, 2001*, p. AIAA 2001-0512.
https://doi.org/10.2514/6.2001-512

31. P. R. Spalart and S. R. Allmaras, “A one-equation turbulence model for aerodynamic flows,” in *30th Aerospace Sciences Meeting and Exhibit, Reno, NV, 1992*, p. AIAA 92–0439.
https://doi.org/10.2514/6.1992-439

32. C. Mockett, M. Fuchs, A. Garbaruk, M. Shur, P. Spalart, M. Strelets, F. Thiele, and A. Travin, “Two non-zonal approaches to accelerate RANS to LES transition of free shear layers in DES,” in *Progress in Hybrid RANS-LES Modelling*, Ed. by S. Girimaji, W Haase et al., Notes on Numerical Fluid Mechanics and Multidisciplinary Design, Vol. 130 (Springer, Cham, 2015), pp. 187–201.
https://doi.org/10.1007/978-3-319-15141-0_15

33. F. Nicoud, H. B. Toda, O. Cabrit, S. Bose, and J. Lee, “Using singular values to build a subgrid-scale model for large eddy simulations,” Phys. Fluids **23** (8), 085106 (2011).
https://doi.org/10.1063/1.3623274

34. I. Abalakin, P. Bakhvalov, and T. Kozubskaya, “Edge-based reconstruction schemes for unstructured tetrahedral meshes,” Int. J. Numer. Methods Fluids **81** (6), 331–356 (2016).
https://doi.org/10.1002/fld.4187

35. P. Bakhvalov and T. Kozubskaya, “EBR-WENO scheme for solving gas dynamics problems with discontinuities on unstructured meshes,” Comput. Fluids **157**, 312–324 (2017).
https://doi.org/10.1016/j.compfluid.2017.09.004

36. A. P. Duben, T. K. Kozubskaya, P. V. Rodionov, and V. O. Tsvetkova, “EBR schemes with Curvilinear reconstructions of variables in the near-wall Region,” Comput. Math. Math. Phys. **61** (1), 1–16 (2021).
https://doi.org/10.1134/S0965542520120039

37. P. A. Bakhvalov, “Method of local element splittings for diffusion terms discretization in edge-bases schemes,” KIAM Preprint No. 79 (Keldysh Inst. Appl. Math. Russ. Acad. Sci., Moscow, 2006) [in Russian].
https://doi.org/10.20948/PREPR-2020-79-E

38. Y. Zhang, H. Chen, K. Wang, and M. Wang, “Aeroacoustic prediction of a multi-element airfoil using wall-modeled large-eddy simulation,” AIAA J. **55** (12), 4219–4233 (2017).
https://doi.org/10.2514/1.J055853

39. J. S. Bendat and A. G. Piersol, *Random Data*: *Analysis and Measurement Procedures*, 4th ed. (Wiley, New York, 2010).

40. G. Heinzel, A. Rüdiger, and R. Schilling, “Spectrum and spectral density estimation by the Discrete Fourier transform (DFT), including a comprehensive list of window functions and some new at-top windows” (2002).
http://hdl.handle.net/11858/00-001M-0000-0013-557A-5.

41. J. E. Ffowcs Williams, and D. L. Hawkings, “Sound generation by turbulence and surfaces in arbitrary motion,” Philos. Trans. R. Soc. London. Ser. A: Math., Phys. Eng. Sci. **264** (1151), 321–342 (1969).
https://doi.org/10.1098/rsta.1969.0031

42. P. A. Bakhvalov, T. K. Kozubskaya, E. D. Kornilina, A. V. Morozov, and M. V. Yacobovskii, “Technology of predicting acoustic turbulence in the far-field flow,” Math. Models Comput. Simul. **4** (3), 363–374 (2012).
https://doi.org/10.1134/S2070048212030039

43. M. L. Shur, P. R. Spalart, and M. K. Strelets, “Noise prediction for increasingly complex jets. Part I: Methods and tests,” Int. J. Aeroacoust. **4** (3), 213–245 (2005).
https://doi.org/10.1260/1475472054771376

44. M. L. Shur, P. R. Spalart, and M. K. Strelets, “Noise prediction for increasingly complex jets. Part II: Applications,” Int. J. Aeroacoust. **4** (3), 247–266 (2005).
https://doi.org/10.1260/1475472054771385

45. P. R. Spalart and M. L. Shur, “Variants of the Ffowcs Williams–Hawkings equation and their coupling with simulations of hot jets,” Int. J. Aeroacoust. **8** (5), 477–491 (2009).
https://doi.org/10.1260/147547209788549280